

GFB-MRF: A parallel spatial and Bloch manifold regularized iterative reconstruction method for MR Fingerprinting

Simon Arberet^a, Xiao Chen^a, Boris Mailhé^a, Peter Speier^b, Gregor Kördörfer^b, Mathias Nittka^b, Heiko Meyer^b, Mariappan S. Nadar^a

^a*Digital Technology & Innovation, Siemens Healthineers, Princeton, NJ, USA*

^b*Magnetic Resonance, Siemens Healthineers, Erlangen, Germany*

Abstract

Magnetic Resonance Fingerprinting (MRF) reconstructs tissue maps based on a sequence of very highly undersampled images. In order to be able to perform MRF reconstruction, state-of-the-art MRF methods rely on priors such as the MR physics (Bloch equations) and might also use some additional low-rank or spatial regularization. However to our knowledge these three regularizations are not applied together in a joint reconstruction. The reason is that it is indeed challenging to incorporate effectively multiple regularizations in a single MRF optimization algorithm. As a result most of these methods are not robust to noise especially when the sequence length is short. In this paper, we propose a family of new methods where spatial and low-rank regularizations, in addition to the Bloch manifold regularization, are applied on the images. We show on digital phantom and NIST phantom scans, as well as volunteer scans that the proposed methods bring significant improvement in the quality of the estimated tissue maps.

Keywords: Magnetic resonance imaging, Magnetic Resonance Fingerprinting, image reconstruction, iterative reconstruction

1. Introduction

Magnetic Resonance (MR) Fingerprinting (MRF) is a recent technique [1] for estimating quantitative tissue maps which uses a non-stationary pulse sequence (i.e. the sequence of parameters such as repetition time (TR), flip angle (FA), and inversion time, is changing in each time point) to generate a sequence of continuously changing image contrasts, acquired at a high under-sampling ratio. The name *fingerprinting* comes from the fact that, in order to recover

*The concepts and information presented in this paper are based on research results that are not commercially available.

Email address: `simon.arberet@siemens-healthineers.com` (Simon Arberet)

the quantitative parameters, the acquired contrast signals are matched against a dictionary of precomputed magnetization signal responses called *fingerprints*, by analogy with fingerprints used for forensics. These fingerprints, obtained via Bloch equation simulations, model the possible signal evolutions, given the MR parameter sequence and the possible combinations of tissue parameters (T1, T2, proton density, etc.) expected to be present in the scanned object. The MR sequence uses a non stationary sequence of parameters (FA, TR, sampling pattern, etc.) in order to create spatial and temporal incoherence among the signal responses from different tissue types. While the sequence used in the original MRF article [1] was random or pseudo-random, later results [2] where the sequence was optimized, showed a resulting highly structured sequence.

MRF provides an effective solution for quantitative imaging, but requires a highly undersampled acquisition in order to have a reasonable scanning time. The classical MRF technique [1] obtains the tissue maps by first zero-filling the undersampled k-space and then by performing the fingerprint matching.

Following the initial MRF method [1], new techniques [3, 4] were proposed which exploit the redundancy of the fingerprints in the time domain and combining different time points prior to the fingerprint matching in order to “dealias” the images before the fingerprint matching step. Then, some approaches inspired by compressed sensing [5, 6, 7, 8] improved further the performance of MRF by iteratively removing artefacts by alternating between Bloch manifold projection (aka dictionary matching) and gradient update. In order to compensate for numerical instabilities in the high frequency corners of the k-space where the sampling pattern (usually spiral or radial) is not taking measurements, which can cause checkboarding artefacts, these methods may use an additional low-pass filter at each iteration [9, 6]. Note that the method described in [9] alternates between dictionary matching and low-pass filtering, where the low-pass filter changes across iterations in order to gradually include the high frequencies. However, these methods did not (or not successfully [5, 7]) exploit spatial regularities which are naturally present in images.

On the other hand, low-rank priors have been exploited [10, 11, 12, 13, 14, 15] in order to capture redundancy of the MRF signal in the temporal dimension. These methods are iterative and often computationally intensive as they require to compute multiple singular value decompositions (SVD) [12, 13] or higher-order SVD [14]. Note that the recent patch-based method HD-PROST [14] exploits correlated structure of the spatio-temporal image through local (within a patch), non-local (between similar patches) and contrast (i.e. time) scale using higher-order singular value decomposition (HOSVD). In a sense, this last method exploits some sort of spatial structure but the Bloch manifold (dictionary matching) is not used as a prior in the optimization problem, but only at the end-step in order to generate the T1 and T2 maps from the reconstructed contrast images. The recent method [15] is iteratively and jointly optimizing (locally) low-rank and spatial priors, but as in [14], the dictionary matching is not used as a prior in the optimization problem but only as a final step to convert the MRF image to the tissue parameters.

In this paper, which extends results presented in [16] and [17], we propose an

efficient iterative reconstruction method which, in addition to the Bloch manifold regularization, incorporates low-rank and spatial regularizations. We propose two optimization algorithms to combine these three regularizations (Bloch manifold, low-rank and spatial) in a single algorithm: an incremental gradient proximal algorithm [18] where the regularizations are applied sequentially, and a generalized forward-backward algorithm [19] where the regularizers are applied in parallel. The low-rank prior is not applied as a nuclear norm minimization which would be computationally expensive, but via dictionary SVD compression [3, 6] which is computed offline. As in [11], we set a threshold much below the rank of the dictionary which provides low-rank regularization (at the expense of a negligible increase in the approximation error) and greatly improves computational efficiency of the algorithm. As we will discuss in 2.3 (see also the discussion in [11]), decreasing the rank beyond the dictionary rank has the effect of improving low-rank regularization at the expense of linear projection approximation. Another approach studied in this paper is to compute a low-rank subspace via auto-calibration. In both cases, the approaches have the consequence of reducing the temporal dimension of the optimization variables. Indeed, thanks to this temporal compression, the spatial regularization can now be performed very efficiently in the compressed domain. In this paper we use 2D total variation (TV) as an example regularization via a few iterations of the Chambolle-dual algorithm [20], but other spatial regularizers such as cycle spinning [21, 22] or joint (along the compressed-temporal dimension) could also be applied. We actually tried these last two regularizers in another (internal) study and obtained similar results, however it is beyond the scope of this paper to evaluate different spatial regularizers. The fingerprints matching, also performed in the compressed domain, can be further accelerated via e.g. a kd-tree algorithm as in [6], FGM [23], or other approximate nearest neighbors (ANN) techniques [24] or deep neural networks (DNN) [25, 26, 27], and/or even be skipped for inner iterations as we will see later in section 2.1.

Contributions.

- Our main contribution is to propose two new algorithms for MRF reconstruction which exploit jointly and iteratively three regularizations: Bloch manifold regularization, spatial regularization, and low-rank. To our knowledge it is the first time that these three regularizations are optimized jointly. In particular in [5, 6, 8, 9, 12, 13], no spatial regularization is performed, and in [7, 10, 12, 14, 15] the Bloch manifold projection (i.e. dictionary matching) is not performed iteratively but only as a final stage to convert the MRF image to tissue maps.
- We also propose an autocalibration mechanism to impose low-rank in our iterative algorithm so that the low-rank subspace to be data-driven rather than dictionary driven as in [3].
- We compare the proposed variants of our algorithms on a series of experiments: evaluation on synthetic Brainweb data w.r.t. the sequence length

(from 600 TR to 3000 TR) in the cases with and without added noise to the measurements in order to test the robustness of these algorithms.

- After selecting our best candidate among our proposed methods, we compare our (best) method against four different methods from the state-of-the-art on a series of experiments: on synthetic Brainweb data w.r.t. the sequence length (from 600 TR to 3000 TR) with and without added noise to the measurements, and also on a real phantom scan and a real volunteer scan, and in both cases with and without added noise.

The outline of this paper is as follows: We first present our MRF methods in section 2, i.e. the optimization problem we are trying to solve and our proposed algorithms, the implementation of the low-rank prior, the fingerprint matching, the spatial regularization, and the step-size selection. Then in section 3, we present results of experiments, first on Brainweb digital phantom data for which we have a ground truth and thus can provide quantitative results, and then on NIST phantom [28] and volunteer data. We finish by a discussion on the results and a conclusion.

2. Method

The problem we want to solve is to reconstruct the MRF image $\mathbf{X} \in \mathbb{C}^{N \times L}$ assuming a discretization into N voxels, from the observed sequence of length L of k-space samples $\mathbf{Y} \in \mathbb{C}^{S \times L}$, where S is the number of samples per readout. In a second step, the quantitative parameters (T1, T2, ...) can then be retrieved from this image by fingerprint matching (or other regression technique) as described in section 2.4.

As in AIR-MRF [6], we rely on a SVD compression dictionary technique [3] which exploits the compressible (low-rank) structure of the dictionary and has the additional advantages of 1) reducing the size of the optimization variables and thus accelerates and simplifies the optimization problem, 2) accelerating the Fourier transform and gridding operations which are the most costly operations of the algorithm when the k-space trajectory is non Cartesian and multiple coils are used. Indeed, as compression commutes with the Fourier transform and gridding operations, the two operations can be performed much more efficiently in the compressed domain of size k ($k \ll L$) than in the original domain of length L . As we will see later, SVD compression has other advantages.

Let's denote the MRF images after compression by $\mathbf{X}_c \triangleq \mathcal{C}(\mathbf{X}) \in \mathbb{C}^{N \times k}$. Our approach consists of first solving optimization problem (1) to estimate the denoised MRF images, and then retrieving the corresponding tissue parameters via fingerprint matching. Optimization problem (1) is:

$$\begin{aligned} \underset{\hat{\mathbf{X}}_c \in \mathbb{C}^{N \times k}}{\operatorname{argmin}} \quad & \|\mathbf{Y} - \mathcal{G}(\hat{\mathbf{X}}_c)\|_2^2 + \lambda \mathcal{R}(\hat{\mathbf{X}}_c) & (1) \\ \text{subject to } & \hat{\mathbf{X}}_{c(i,:)} \in \mathcal{D}_c, \quad i = 1, \dots, N, \end{aligned}$$

where $\mathcal{G} \triangleq \mathcal{M}\mathcal{F}\mathcal{S}\mathcal{C}^H = \mathcal{M}\mathcal{C}^H\mathcal{F}\mathcal{S}$ is the observation operator, \mathcal{S} the coil sensitivity map, \mathcal{F} the Fourier transform, and \mathcal{M} the undersampling operator. Note that, as shown in [13], the compression operator \mathcal{C} commutes with the Fourier operator, and thus the number of Fourier transforms can be reduced drastically by performing them in the compressed domain. In our implementation, sampling is performed with a series of single-shot spiral trajectories in k-space, and \mathcal{M} and \mathcal{F} together are implemented with a non-uniform fast Fourier transform (NUFFT) [29].

\mathcal{R} is a regularization operator which in our case enforces spatial regularization e.g. using a total variation (TV) regularization. \mathcal{D}_c is the cone of the Bloch response manifold after compression. The Bloch manifold is indeed a cone as it is stable to nonnegative scaling (the proton density in our case) [5], and its SVD compression is a linear projection of a cone which is still a cone. This Bloch manifold projection will be denoted by $\mathcal{P}_{\mathcal{D}_c}$ in the rest of the paper and the details of this projection will be discussed in section 2.4. Note that the Bloch manifold is not convex, and moreover its projection is usually implemented via fingerprint matching, i.e. a non-smooth (non differentiable) projection.

In the following, we propose different variants of the CS-MRF method. These variants and their names are summarized in Table 1.

2.1. Incremental gradient proximal MRF (IGP-MRF)

In order to solve optimization problem (1), we can rely on the *incremental (sub)gradient-proximal method* (IGP) [18, equations 2.3 and 2.4]. Algorithm 1 is an IGP algorithm that optimizes the image volume in the compressed domain, as well as the tissue parameters $\hat{\theta} = \{T1, T2, \dots\}$ and the proton density $\hat{\rho}$, which are obtained during the fingerprint matching step (will be described in section 2.4). The strategy for the gradient step size α_k will be discussed in section 2.6. Note that \mathcal{G}^H denotes the adjoint of operator \mathcal{G} . As will be explained in section 2.3, the low-rank prior imposes the solution to be in a low-dimensional subspace which approximates the Bloch manifold. As a consequence, this prior might be enough to replace the fingerprint matching as a regularizer (in a similar way as in [12] and [11]). In that case we could skip the fingerprint matching except at the final iteration to retrieve the tissue maps. Note that if the fingerprint matching/Bloch manifold projection is skipped in optimization problem (1), then this problem becomes smooth and convex (as only the Bloch manifold projection is non-convex and non-smooth) for which many algorithms and nice convergence properties exist. Then Algorithm 1 with skipped fingerprint matching reduces to the well known (convex) gradient-proximal algorithm. In practice we also notice that, in the case we drop the fingerprint matching in the iterative procedure, it is still useful to have the first matching at the first iteration as it provides a good initialization. The variants without matching are denoted IGP-MRF-00 and IGP-MRF-10 in Table 1. These methods were first introduced in our ISMRM abstract [16] where they were denoted CS-MRF.

Algorithm 1: IGP-MRF algorithm

* for methods IGP-MRF-01 and IGP-MRF-10, the fingerprint matching step is applied only in the first and last iteration.

Input: \mathbf{Y} , λ .

Initialize:

$k := 0$, $\hat{\mathbf{X}}_c^{(0)} := 0$.

while $k < K_{max}$ **do**

Gradient update:

$\mathbf{Z}_c := \hat{\mathbf{X}}_c^{(k)} - \alpha_k \mathcal{G}^H(\mathcal{G}(\hat{\mathbf{X}}_c^{(k)}) - \mathbf{Y})$

Fingerprint matching*:

$[\mathbf{Z}_c, \hat{\theta}, \hat{\rho}] := \mathcal{P}_{\mathcal{D}_c}(\mathbf{Z}_c)$

Spatial regularization:

$\hat{\mathbf{X}}_c^{(k+1)} := \text{prox}_{\alpha_k \lambda \mathcal{R}}(\mathbf{Z}_c)$

$k := k + 1$

end

return $\hat{\mathbf{X}}_c^{(k)}$, $\hat{\theta}$, $\hat{\rho}$

2.2. Generalized forward-backward MRF (GFB-MRF)

We propose another algorithm where the fingerprint matching and the spatial regularization are performed in parallel rather than sequentially. The algorithm is derived from the generalized forward-backward splitting algorithm (GFB) [19] which generalizes the forward-backward algorithm to deal with multiple non-smooth functions (which are two in our case: the indicator function of the Bloch manifold, and the TV norm). As for the forward-backward algorithm, the regularity of the data fidelity term is explicitly used with a gradient step (forward step), and the proximity operators of the non-smooth terms are applied in parallel (backward step). GFB algorithm has nice theoretical properties [19] such as a proven convergence with robustness to errors on the computation of the proximity operators and errors of the gradient of the smooth term. Convergence of GFB are also proven for constant or decreasing step-size. Note that in our case the assumptions of the GFB algorithm are not met, in particular the Bloch manifold is not convex. This method was first introduced in our ISMRM abstract [17].

2.3. Low-rank prior

There exists different ways to impose a rank constraint on the data in a matrix form (sometime called Casorati matrix) $\mathbf{X} \in \mathbb{C}^{N \times L}$. One way is to project the data on the non-convex set of low-rank matrices (i.e. $\{\mathbf{X} \mid \text{rank}(\mathbf{X}) \leq k\}$), using the Eckart-Young theorem and performing a SVD decomposition of the matrix followed by an singular value hard thresholding. Another way is to relax this non-convex constraint to its convex hull, i.e. replacing the rank constraint by the nuclear norm, defined as the sum of the singular values of the matrix. While this approach is convex, it still relies on a costly SVD followed by a soft-thresholding operation. This approach was used in [12].

Algorithm 2: GFB-MRF algorithm

Input: \mathbf{Y} , λ .
 Initialize:
 $k := 0$, $\hat{\mathbf{X}}_c^{(0)} := 0$, $\mathbf{Z}_{bloch}^{(0)} := 0$, $\mathbf{Z}_{spat}^{(0)} := 0$.
while $k < K_{max}$ **do**
 Gradient update:
 $\mathbf{G} := \hat{\mathbf{X}}_c^{(k)} - \alpha_k \mathcal{G}^H(\mathcal{G}(\hat{\mathbf{X}}_c^{(k)}) - \mathbf{Y})$
 Fingerprint matching:
 $\mathbf{Z}_{bloch}^{(k+1)} := \mathcal{P}_{\mathcal{D}_c}(\mathbf{G} + \mathbf{O}_{bloch}) - \mathbf{O}_{bloch}$
 with $\mathbf{O}_{bloch} = \hat{\mathbf{X}}_c^{(k)} - \mathbf{Z}_{bloch}^{(k)}$
 Spatial regularization:
 $\mathbf{Z}_{spat}^{(k+1)} := \text{prox}_{\alpha_k \lambda \mathcal{R}}(\mathbf{G} + \mathbf{O}_{spat}) - \mathbf{O}_{spat}$
 with $\mathbf{O}_{spat} = \hat{\mathbf{X}}_c^{(k)} - \mathbf{Z}_{spat}^{(k)}$
 Merging:
 $\hat{\mathbf{X}}_c^{(k+1)} := (\mathbf{Z}_{bloch}^{(k+1)} + \mathbf{Z}_{spat}^{(k+1)}) / 2$
 $k := k + 1$
end
Fingerprint matching:
 $[\hat{\mathbf{X}}_c^{(k+1)}, \hat{\theta}, \hat{\rho}] := \mathcal{P}_{\mathcal{D}_c}(\hat{\mathbf{X}}_c^{(k)})$
return $\hat{\mathbf{X}}_c^{(k+1)}, \hat{\theta}, \hat{\rho}$

Low-rank via SVD compression. Another way to impose low-rank is via a low-rank factorization of \mathbf{X} [30, 11], i.e. instead of searching for an optimal matrix \mathbf{X} having a low-rank, we are searching for two matrices $\tilde{\mathbf{U}} \in \mathbb{C}^{N \times k}$ and $\tilde{\mathbf{V}}^H \in \mathbb{C}^{k \times L}$ with $k < N$ and $k < L$, and such that $\mathbf{X} = \tilde{\mathbf{U}}\tilde{\mathbf{V}}^H$. While optimizing jointly the two matrices $\tilde{\mathbf{U}}$ and $\tilde{\mathbf{V}}^H$ is not convex, in some problems one of these two matrices can be fixed with some a priori knowledge. In that case the problem is simplified and becomes convex. As the rows of \mathbf{X} are supposed to be in the cone of the Bloch response manifold according to the MR physics, and that this cone is contained in a relatively low dimensional subspace, the principal temporal components of the Bloch signal dictionary $\tilde{\mathbf{V}}_d$ can be used to form the matrix $\tilde{\mathbf{V}}$ (conjugate transpose of $\tilde{\mathbf{V}}^H$). In this case, $\mathbf{X}_c \triangleq \mathcal{C}(\mathbf{X}) = \mathcal{C}_d(\mathbf{X}) \triangleq \mathbf{X}\tilde{\mathbf{V}}_d$, where $\tilde{\mathbf{V}}_d$ is obtained by keeping the k first right singular vectors (i.e. the k first columns of \mathbf{V}_d) of the dictionary \mathbf{D} , where $\mathbf{D} = \mathbf{U}_d \mathbf{S}_d \mathbf{V}_d^H$ is the SVD decomposition of \mathbf{D} . This idea was used in previous work [6], where SVD compression was used with a rather large rank (200, i.e. larger than the rank of the dictionary) in order to reduce dimensionality and speeding up the NUFFT and matching time, but not to impose a low-rank constraint. In [11] this idea of imposing a low-rank constraint via this approach was used with a rank value of around $k = 6$ to 10. In this paper we used a value of $k = 10$ for all our proposed methods (shown in Table 1) and experiments. To choose this value, we performed experiments for different values of k and noticed that the best

performance were in the range 10 to 20, and started to degrade for values smaller than 10. So as smaller the value faster the reconstruction, the value of $k = 10$ was a selected.

All of our proposed methods in Table 1 use a dictionary SVD compression. We also propose in the next paragraph another approach which in addition to the dictionary SVD compression exploits auto-calibration data to impose a low-rankness.

Low-rank via autocalibration. We propose an approach where the decompression matrix $\tilde{\mathbf{V}}^H$ is the product of two matrices $\tilde{\mathbf{V}}_{ac}$ and $\tilde{\mathbf{V}}_d$, i.e. $\tilde{\mathbf{V}}^H = (\tilde{\mathbf{V}}_d \tilde{\mathbf{V}}_{ac})^H$, and $\mathbf{X}_c = \mathcal{C}(\mathbf{X}) = \mathbf{X}\tilde{\mathbf{V}} = \mathbf{X}\tilde{\mathbf{V}}_d\tilde{\mathbf{V}}_{ac}$. The matrix $\tilde{\mathbf{V}}_d \in \mathbb{C}^{L \times r}$ is the fingerprint dictionary compressed to its rank value r , while matrix $\tilde{\mathbf{V}}_{ac} \in \mathbb{C}^{r \times k}$ is the result of an auto-calibration data and k is the desired low-rank value. More formally, if $\mathbf{D} \in \mathbb{C}^{N \times L}$ is the uncompressed dictionary matrix, it admits an SVD decomposition $\mathbf{D} = \mathbf{U}_d \mathbf{S}_d \mathbf{V}_d^H$, from which we obtain the dictionary SVD compression matrix $\tilde{\mathbf{V}}_d$ by taking the r first right singular vectors (i.e. the r first columns of \mathbf{V}_d). The auto-calibration data can be obtained directly in the compressed domain ($\mathbf{X}_{ac} = \mathcal{C}_d(\mathbf{X}_a) \in \mathbb{C}^{N \times r}$, with $\mathbf{X}_a \in \mathbb{C}^{N \times L}$), by for example running one iteration of AIR-MRF (i.e. one iteration of algorithm 1 without the spatial regularization or similarly method [3]), or compressed afterwards using the dictionary compression matrix $\tilde{\mathbf{V}}_d$. Note that in the first case, the data is in the Bloch manifold because a fingerprint matching (i.e. a Bloch manifold projection) has been performed as the last step of this algorithm. This is, however, different than using the dictionary for low-rank compression as in section 2.3 because the distribution of the estimated tissues reflects what is (or rather what has been estimated to be) in the data as opposed to the fingerprint dictionary which is defined by a pre-chosen set of tissue parameters. In other words, the possible errors in this autocalibration only concern the distribution of the tissues, but not the fingerprint signals themselves, because the fingerprints are still coming from the dictionary. We can then obtain the auto-calibration compression matrix $\tilde{\mathbf{V}}_{ac}$ by performing an SVD decomposition on the compressed auto-calibration data $\mathcal{C}_d(\mathbf{X}_a) = \mathbf{X}_a \tilde{\mathbf{V}}_d = \mathbf{U}_{ac} \mathbf{S}_{ac} \mathbf{V}_{ac}^H$, and keeping the k first right singular vectors (i.e. the k first columns of \mathbf{V}_{ac}).

The variants of our methods with auto-calibration are denoted IGP-MRF-10 and IGP-MRF-11 in Table 1. The variants with and without auto-calibration will be evaluated in section 3.2 (see methods IGP-MRF-00 vs IGP-MRF-10 and methods IGP-MRF-11 vs IGP-MRF-01 in Table 1 and Figure 1).

2.4. Fingerprint matching

There are different techniques for fingerprint matching or more generally tissue parameters regression which are briefly discussed at the end of this section; however, the goal of this paper is not on the fingerprint matching technique, so we decided to rely on the classical matching technique [1] for this study. The fingerprint matching consists of finding the most correlated fingerprint \hat{k}_i in the

dictionary for each voxel i , i.e.

$$\hat{k}_i = \operatorname{argmax}_k \frac{|\langle \mathbf{D}_{c(k,:)}, \hat{\mathbf{X}}_{c(i,:)} \rangle|}{\|\mathbf{D}_{c(k,:)}\|_2}. \quad (2)$$

The proton density can then be estimated using the following equation:

$$\hat{\rho}_i = \max \left\{ \frac{\Re \langle \mathbf{D}_{c(\hat{k}_i,:)}, \hat{\mathbf{X}}_{c(i,:)} \rangle}{\|\mathbf{D}_{c(\hat{k}_i,:)}\|_2^2}, 0 \right\}, \quad (3)$$

where $\Re(\cdot)$ denotes the real part, \mathbf{D}_c is the discretized dictionary after compression ($\mathbf{D}_c = \mathbf{D}\tilde{\mathbf{V}}_d$), and $\mathbf{D}_{c(k,:)}$ is the k -th fingerprint of the discretized dictionary. Note that the fingerprint matching can be performed directly in the compressed domain since the dictionary decompression (adjoint of the compression operator) is an isometry (i.e. $\langle \mathbf{D}_{c(k,:)}\tilde{\mathbf{V}}_d^H, \hat{\mathbf{X}}_{c(i,:)}\tilde{\mathbf{V}}_d^H \rangle = \langle \mathbf{D}_{c(k,:)}, \hat{\mathbf{X}}_{c(i,:)} \rangle$, and $\|\mathbf{D}_{c(k,:)}\tilde{\mathbf{V}}_d^H\|_2 = \|\mathbf{D}_{c(k,:)}\|_2$).

In the case we use the low-rank variant of the methods with auto-calibration data (described in section 2.3, i.e. methods IGP-MRF-10 and IGP-MRF-11), the previous formulas (2) and (3) need to take into account the auto-calibration compression matrix. As $\langle \mathbf{D}_{c(k,:)}\tilde{\mathbf{X}}_{c(i,:)}\tilde{\mathbf{V}}_{ac}^H \rangle = \langle \mathbf{D}_{c(k,:)}\tilde{\mathbf{V}}_{ac}, \hat{\mathbf{X}}_{c(i,:)} \rangle$, we actually don't need to uncompress the data $\hat{\mathbf{X}}_{c(i,:)}$ with $\tilde{\mathbf{V}}_{ac}^H$ prior to the fingerprint matching and can instead apply (only once) the compression operator $\tilde{\mathbf{V}}_{ac}$ on the dictionary. So that with auto-calibration, formulas (2) and (3) need then to be replaced by:

$$\hat{k}_i = \operatorname{argmax}_k \frac{|\langle \mathbf{D}_{c(k,:)}\tilde{\mathbf{V}}_{ac}, \hat{\mathbf{X}}_{c(i,:)} \rangle|}{\|\mathbf{D}_{c(k,:)}\|_2},$$

$$\hat{\rho}_i = \max \left\{ \frac{\Re \langle \mathbf{D}_{c(\hat{k}_i,:)}\tilde{\mathbf{V}}_{ac}, \hat{\mathbf{X}}_{c(i,:)} \rangle}{\|\mathbf{D}_{c(\hat{k}_i,:)}\|_2^2}, 0 \right\} \quad (4)$$

Once the fingerprint \hat{k}_i is identified, the quantitative tissue values $\hat{\theta}_i = \{\text{T1}_i, \text{T2}_i, \dots\}$ are obtained by a simple look-up table (LUT): $\hat{\theta}_i = \text{LUT}(\hat{k}_i)$, while the proton density is obtained by equations (3) (if no auto-calibration) or (4) (if auto-calibration). The contrast image is then re-synthesized by multiplying the proton density with the selected atom as follows: $\hat{\mathbf{X}}_{c(i,:)}^{new} := \hat{\rho}_i \mathbf{D}_{c(\hat{k}_i,:)}$, and including the auto-calibration compression in the case of the auto-calibration variant: $\hat{\mathbf{X}}_{c(i,:)}^{new} := \hat{\rho}_i \mathbf{D}_{c(\hat{k}_i,:)}\tilde{\mathbf{V}}_{ac}$.

Rather than selecting the most correlated fingerprint by exhaustive search, fingerprint matching can be accelerated with approximate k-nearest-neighbour (ANN) techniques as in AIR-MRF [6] where a kd-tree is used. Other fast matching techniques have been developed specially for MRF such as the Fast Group Matching (FGM) [23] or neural networks [25, 26, 27]. However, the choice of the accelerated matching technique is beyond the scope of this paper and only exhaustive search was used for all the reconstruction methods tested in section 3.

2.5. Spatial regularization

Spatial regularization (term $\mathcal{R}(\hat{\mathbf{X}}_c)$ in Eq. (1)) is applied via its proximal operator [31] in the compressed domain, on each image slice of $\hat{\mathbf{X}}_c$. Because the low-rank value k is small (in the order of 10) compared to the sequence length L (in the order of 10^3), the regularization is quite efficient. We choose to use an isotropic TV regularization using Chambolle algorithm [20], because it converges very fast in the first iterations, and thus provides a good approximation of the TV proximal operation after just a few iterations. Other efficient spatial regularization such as cycle spinning [21, 22] can be used instead. Joint (along the compressed-temporal dimension) TV sparse regularization also provides similar performance in our experience.

2.6. Step-size selection

Selection of the step size is important to ensure convergence and good reconstruction performance. Forward backward algorithm is known to converge for $\alpha < 2/L(\nabla f)$, where $L(\nabla f)$ denotes the Lipschitz constant of the gradient of f . In our case, $f = \frac{1}{2}\|\mathcal{G}(\hat{\mathbf{X}}_c) - \mathbf{Y}\|_2^2$ and thus $L(\nabla f)$ is simply the spectral radius of $\mathcal{G}^H\mathcal{G}$ which should be equal to one if the (non-uniform) Fourier transform and sampling operations were properly normalized and compensated. In practice, one rarely has an accurate knowledge of $L(\nabla f)$ and also this condition is conservative in that it focuses on the worst case. It is thus usually better in practice to start with a relatively large step size to converge quickly but at the same time ensure stability of the iterations with a backtracking rule as explained in section 2.6.2. The drawback of a backtracking rule, however, is that it usually increases significantly the computation load of the algorithm.

Previous work on step-size selection in the context of iterative MRF reconstruction, such as in BLIP [5] and AIR-MRF [6], suggested that a large step size (larger than $\alpha = 1$) ensures faster convergence and leads to significantly better results. In [5], the proposed heuristic is to start with a step size equals to the undersampling ratio e.g. $\alpha = N/S$ and then to use a backtracking rule similar to the one presented in section 2.6.2.

2.6.1. Rescaling step-size

In AIR-MRF [6], if $\alpha > 0$ is the original step size, the first iteration of AIR-MRF leads to $\hat{\mathbf{X}}_c^{(1)} = \mathcal{P}_{\mathcal{D}_c}(\alpha\mathcal{G}^H\mathbf{Y}) = \alpha\mathcal{P}_{\mathcal{D}_c}(\mathcal{G}^H\mathbf{Y})$ because of the positive homogeneity property of the orthogonal projection onto a cone (the Bloch manifold). As a result, the step size α of the first iteration can be chosen at the end of the first iteration, after the matching step. Moreover, it can be chosen optimally by minimizing the data fidelity term: $\|\alpha\mathcal{G}(\tilde{\mathbf{X}}_c^{(1)}) - \mathbf{Y}\|_2^2$ with $\tilde{\mathbf{X}}_c^{(1)} = \mathcal{P}_{\mathcal{D}_c}(\mathcal{G}^H\mathbf{Y})$, where closed form solution is $\alpha = \Re\left(\langle \mathbf{Y}, \mathcal{G}(\tilde{\mathbf{X}}_c^{(1)}) \rangle\right) / \|\mathcal{G}(\tilde{\mathbf{X}}_c^{(1)})\|_2^2$. We call this procedure which is used in all our proposed methods (see Table 1): *rescaling step-size* and use it as an heuristic to select the step size at the first iteration and subsequent iterations until a backtracking rule is possibly applied.

2.6.2. Backtracking strategy

Convergence can be guaranteed via a backtracking line search. In general, such method proceeds by first checking a condition at the end of each iteration. The so-called backtracking condition enforces that the objective has decreased “sufficiently”. If this condition fails, the stepsize is decreased and the current iteration is restarted until the backtracking condition holds. The backtracking rule described here is the same in AIR-MRF and inspired by the one of IHT [32, 5, 6]. The backtracking condition is that if either *condition a* or *condition b* defined below is false, then the candidate update is rejected, and the iteration is restarted with the step size halved.

condition a:

$$\alpha \leq 0.99 \frac{\left\| \hat{\mathbf{X}}_c^{(k+1)} - \hat{\mathbf{X}}_c^{(k)} \right\|_2^2}{\left\| \mathcal{G}^H \mathcal{G} \left(\hat{\mathbf{X}}_c^{(k+1)} - \hat{\mathbf{X}}_c^{(k)} \right) \right\|_2^2}$$

condition b:

$$\left\| \mathcal{G}^H \mathbf{Y} - \mathcal{G}^H \mathcal{G} \hat{\mathbf{X}}_c^{(k+1)} \right\|_2^2 \geq \left\| \mathcal{G}^H \mathbf{Y} - \mathcal{G}^H \mathcal{G} \hat{\mathbf{X}}_c^{(k)} \right\|_2^2$$

The iteration is repeated until both conditions are met. In the following, we call *backtracking* (BT) the strategy consisting of rescaling the step size (as described in 2.6.1) in the first iteration and then applying the backtracking rule just described.

2.6.3. Rescaling fixed step-size

We call *Rescaling fixed step-size* strategy (FSZ) the strategy consisting of rescaling the step size (as described in 2.6.1) and then keeping the step size fixed for the remaining iterations.

These step-size strategies will be evaluated in the next section where variants of the same method with FSZ or with BT strategy will be compared (see e.g. methods IGP-MRF-01 and IGP-MRF-01BT in Table 1).

3. Experiments

We studied the different MRF algorithms on the Brainweb digital phantom data [33] in order to perform a quantitative analysis of the performance. Brainweb digital phantom being the only data for which we have a ground truth. We then showed results on real acquisition, on the NIST phantom in section 3.3 and on a real volunteer brain data in section 3.4. We studied the performance when the raw measurements are noise-free, and when the measurements were contaminated with some noise in order to make the experiment more realistic and study the robustness of the algorithms. We compared in section 3.2 our proposed methods and their variants (summarized in Table 1) which perform spatial regularization and showed that GFB-MRF is the best method. We also compared GFB-MRF with other methods such as the classical MRF [1], AIR-MRF [6], kt-SVD-MRF [34], and Zhao et al. LR [11]. In all the cases, the

Table 1: Proposed methods

name of the method	optimization algorithm	auto-calibration	matching at every iteration	step-size strategy
IGP-MRF-01	algo 1	no	yes	FSZ
IGP-MRF-01BT	algo 1	no	yes	BT
IGP-MRF-00	algo 1	no	no	BT
IGP-MRF-10	algo 1	yes	no	BT
IGP-MRF-11	algo 1	yes	yes	FSZ
GFB-MRF	algo 2	no	yes	BT

results of our proposed methods were shown for the iteration which obtained the lowest data fidelity error $\|\mathbf{Y} - \mathcal{G}(\hat{\mathbf{X}}_c)\|_2^2$, which is usually obtained after 5 to 10 iterations, and a SVD compression of $k = 10$ as explained in section 2.3.

The performance is measured in terms of relative error in the tissue map estimation, i.e. if $\hat{\theta}_n$ is the estimated tissue parameter (T1 or T2) map at pixel location n , and θ_n is the ground truth tissue parameter map at the same pixel location, then the error is calculated as: $\frac{1}{N} \sum_n |\hat{\theta}_n - \theta_n|/\theta_n$. Note that a mask is applied so that the background is discarded in the error calculation.

3.1. MRF Acquisitions

All the experiments of this paper (both the synthetic on Brainweb, and the real scans) were obtained using the following prototype pulse sequence: After the application of an inversion pulse and an inversion time (TI) of 21 ms the FISP acquisition started. Here, the flip angle (FA) and the repetition time (TR) varied for each echo. TR ranged from 12.1 ms to 15.0 ms and the FA ranged from 0° to 74° while the echo time was constant (2 ms). Each echo encoded an image by a single spiral readout with a variable density k-space trajectory as described in [35], using an inner and outer undersampling ratio of 24 and 48 respectively. The spiral readout had approx. 6 ms duration for the default parameters (FOV 256, matrix 256, dwell time $2.5 \mu\text{s}$, 48 spiral interleaves for full sampling) and was followed by gradients rewinding the moments on the x- and y-axis. In order to improve the incoherence of resulting undersampling artefacts, the spiral trajectory was rotated by 82.5° (84° every 48 interleaves) from TR to TR [36].

A long sequence of length 3000 TRs was acquired and used as a reference to compare the different methods which were evaluated on shorter sequences (e.g. of length 1000 TRs for the real acquisition experiments, and from 600 to 2000 TRs for the Brainweb experiment) obtained by retrospectively discarding data from the end of the original sequence. The constructed dictionary consisted of 5366 atoms with T1 ranging from 10 to 4500 ms (increments of 10, 20, 40, and 100 for ranges 10 to 100, 120 to 1000, 1040 to 2000, and 2050 to 4500, respectively, in ms) and T2 ranging from 2 to 3000 ms (increments of 2, 5, 10, 50, 100, and 200 for ranges 2 to 10, 15 to 100, 110 to 300, 350 to 800, 900 to

1600, and 1800 to 3000, respectively, in ms), excluding combinations of T1 and T2 values where $T1 < T2$.

3.2. Brainweb digital phantom evaluations

In the following experiments, the digital phantom from Brainweb [33] was used with ground truth T1, T2 and proton density (PD) maps at a field strength of 1.5 T, zero padded to be square. The 434×434 image is nearest-neighbor downsampled to 256×256 . Bloch responses for both dictionary generation and generation of simulated data were calculated from ground truth values using Bloch simulations. Note that as described in section 3.1 only one spiral is acquired per time point. The (simulated) data in this section is single coil while the real scan acquisitions in the next sections are multi-coils. The methods are evaluated for different sequence lengths (by retrospectively discarding the end of the original sequence) ranging from 600 TRs to 3000 TRs.

3.2.1. Noise-free measurements

We first studied the performance of our methods with respect to the sequence length on noise-free Brainweb digital phantom data. Results (not reported) showed that our proposed methods (summarized in table 1) performed quite similarly in the noise-free case. The pulse sequence and dictionary used is described in section 3.1.

The regularization parameter was set to $\lambda = 10^{-4}$ for all the methods, which is the optimal value we obtained by swiping this parameter value. The reasons we chose a fix value for all the sequence lengths and variants are: 1) these algorithms solve the same optimization problem (Equation (1)), and 2) we want to see if a method is more robust or sensitive to this parameter when the conditions of the experiment change slightly (the sequence length is changing but the SVD compression rank k remains the same). When we will add a little noise in section 3.2.2 this parameter will be set slightly higher as this parameter should be proportional to the noise std [37].

3.2.2. Influence of noise

In this experiment (see Figure 1), we want to assess the robustness of the methods with respect to noise in the measurements. We followed the same experimental setup as in section 3.2.1, but with a (zero mean) Gaussian noise added to the raw measurements. The standard deviation of the noise was set to be equal to 0.1% of the value of the largest sample of the raw measurement. The regularization parameter was set to $\lambda = 5 \times 10^{-4}$ for all the methods, which is the optimal value we obtain by swiping this parameter value.

Results with noisy measurements, depicted in Figure 1, show that GFB-MRF obtained the best results on both T1 and T2 map estimation for (almost) all the sequence lengths.

We compared GFB-MRF which obtained globally the best results in the previous experiment (see Figure 1) with the classical MRF [1], AIR-MRF [6], kt-SVD-MRF [34], and Zhao et al. LR [11]. For the last method, we set the low-rank value to $k = 8$ as suggested by the authors [11]. Note that we also tested

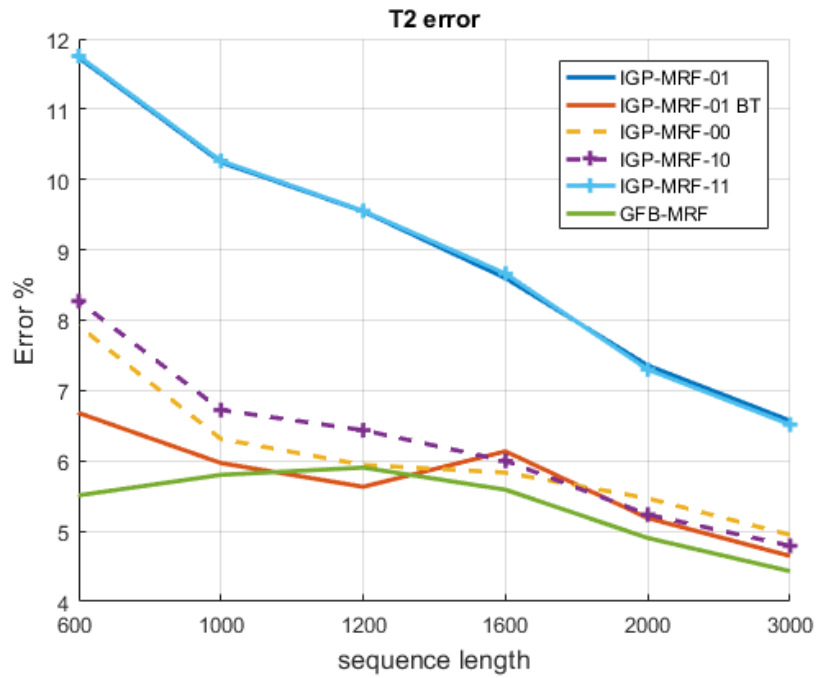
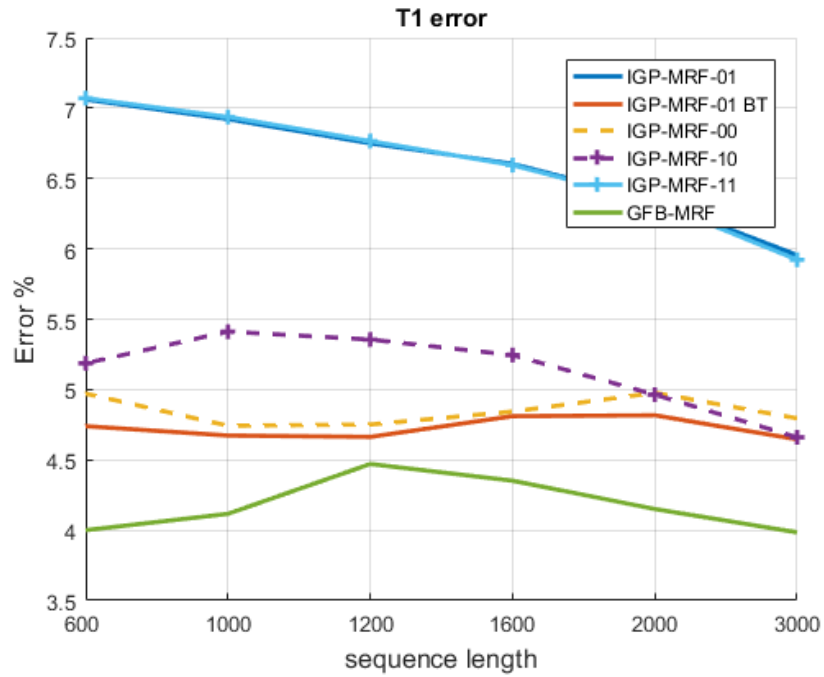


Figure 1: T1 (top) and T2 (bottom) errors w.r.t. sequence length of proposed methods on Brainweb digital phantom data with noisy measurements

Zhao et al. method with $k = 10$ in order to select the same rank thresholding value as for our methods and the results were very similar (but slightly worse) as with $k = 8$.

The performance of the different algorithms on noise-free Brainweb digital phantom data are depicted in Figure 2, and the performance of the different algorithms on Brainweb digital phantom data with noisy measurements are depicted in Figure 3.

GFB-MRF performed much better than the classical MRF method and the other compared methods (MRF, AIR-MRF, Zhao-LR, kt-SVD-MRF) in both noise-free and noisy case and for all the sequence lengths. As an example, GFB-MRF reduced the T1 error from 2.1% to 1.3% and the T2 error from 4.5% to 2.7% compared to AIR-MRF, Zhao-LR, and kt-SVD-MRF at a sequence length of $L=600$ in the noiseless case, and the T1 error from 7.5% to 4% and the T2 error from 12.5% to 5.5% compared to the classical MRF, AIR-MRF, and kt-SVD-MRF at a sequence length of $L=600$ in the added noise case. We also noted that AIR-MRF, Zhao-LR and kt-SVD-MRF perform significantly better than the original MRF method in the noise-free case, but that in the noisy scenario they all performed similarly as the classical MRF except Zhao-LR [11] which performed worse.

3.3. NIST phantom evaluations

In this section, we studied the performance of our proposed GFB-MRF method and other competitive methods on the NIST phantom [28], 1) in the noise-free case (Figure 4), and 2) with additional Gaussian noise added to the measurements as described in section 3.2.2 (Figure 5). Zoom on these images are also depicted in the supporting document. We used the colormap specifically defined for MRF in [38]. NIST phantom was scanned using the sequence of section 3.1 cropped to a length of $L = 1000$ TRs on a MAGNETOM Skyra 3T scanners (Siemens Healthcare, Erlangen, Germany).

As a reference, we also showed in the supporting document the results of the original MRF and AIR-MRF at a longer sequence length $L=3000$ TRs. Note that it is a reference but not the ground truth. Indeed, as can be observed with Brainweb digital phantom data (in section 3.2), results at $L=3000$ TRs are better than those from a shorter sequence length, but there still exists a significant error at $L=3000$ TRs. Note also that the water inside the NIST phantom results in flow artefacts, which explains the non-uniform signal in the background which just contains water. We can see in Figure 4 that in the noise-free case, the other methods were able to correct the artefacts of original MRF method on the T2 map, and that our proposed GFB-MRF method was able to further remove ringing artefacts. Note that kt-SVD-MRF overestimated the PD map.

In the noisy case (Figure 5), our proposed GFB-MRF method is the only method that was able to get rid of the noise and estimate maps that look similar to the reference.

The values and standard deviations (std) of the three regions of interest (ROI) corresponding to the three ROIs of the zoomed NIST image depicted in

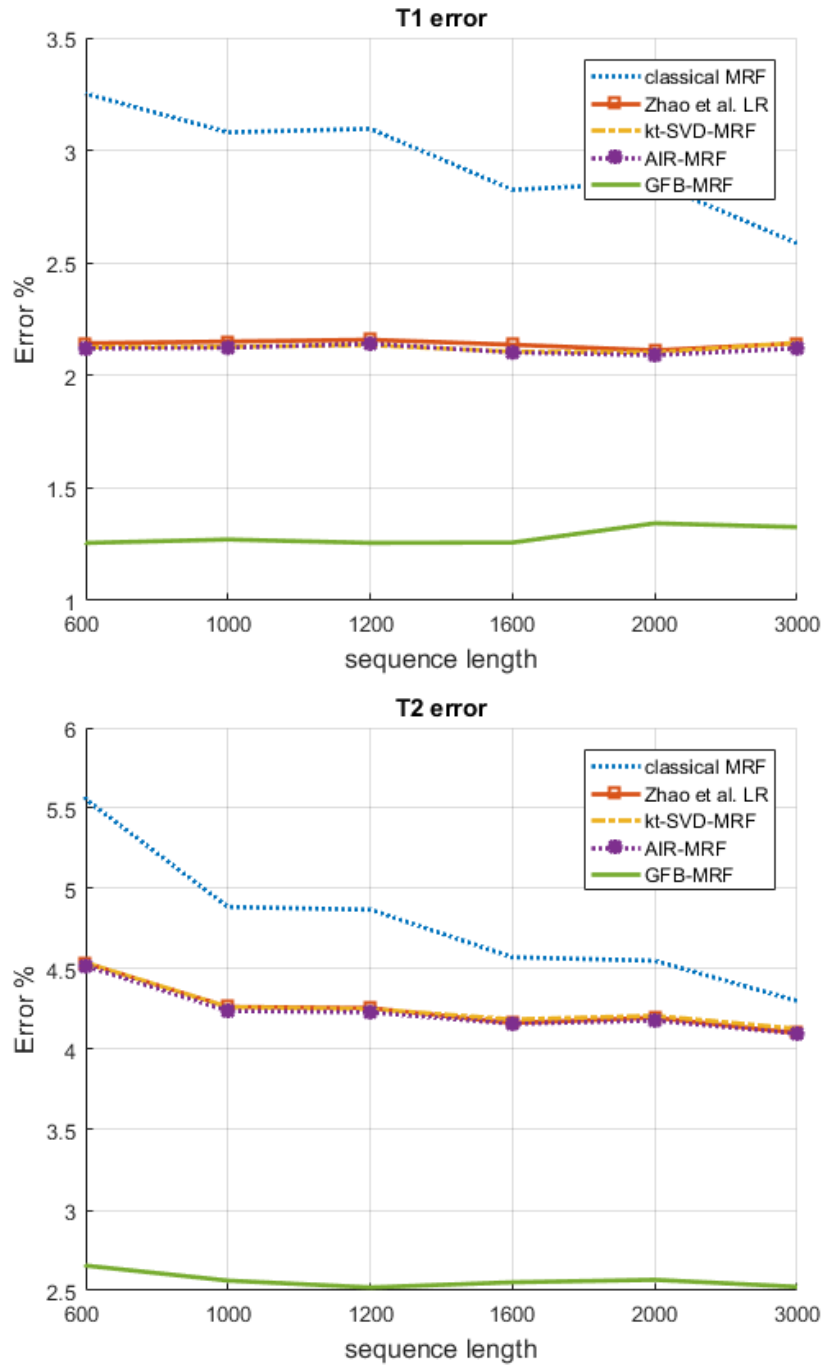


Figure 2: T1 (top) and T2 (bottom) errors w.r.t. sequence length of proposed GFB-MRF method compared to other methods on Brainweb digital phantom data with noise-free measurements

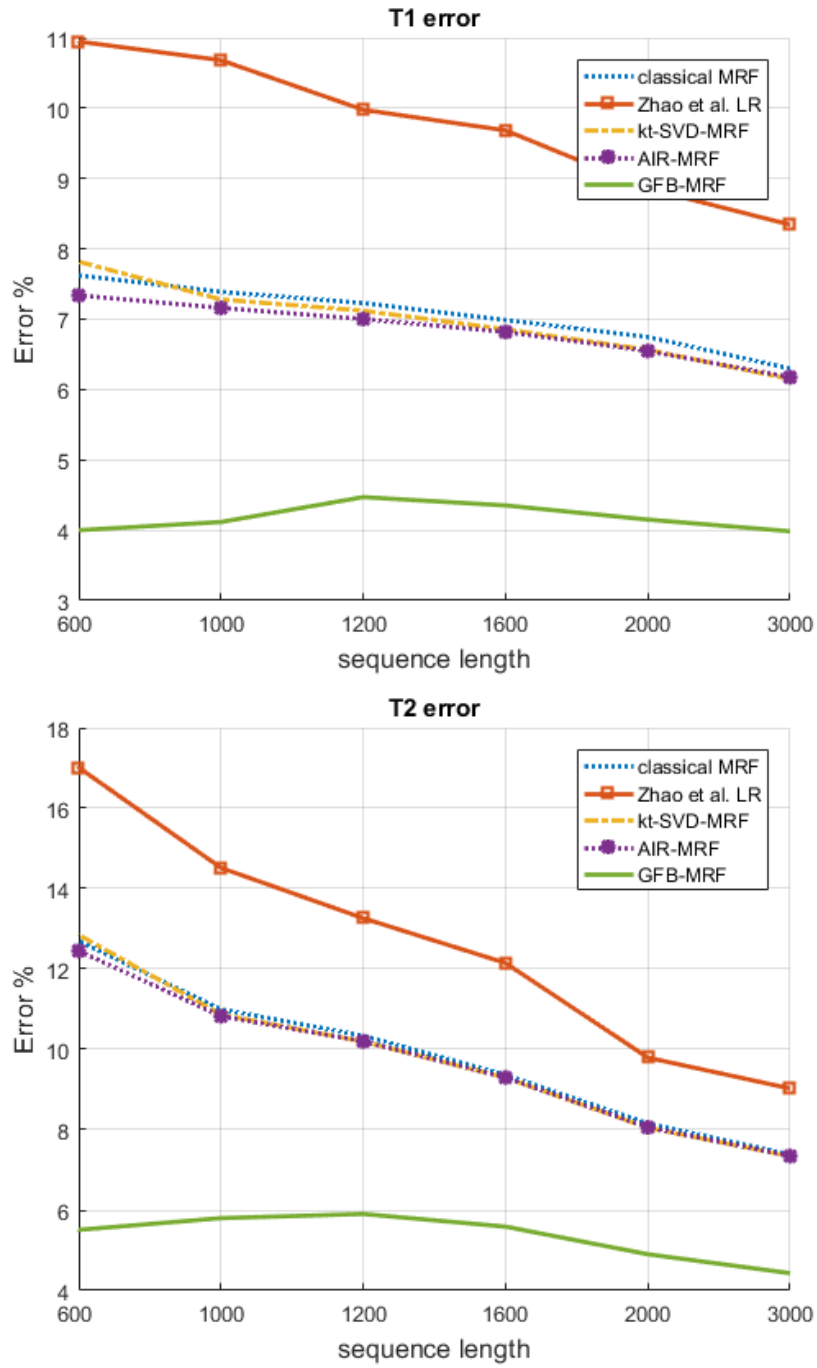


Figure 3: T1 (top) and T2 (bottom) errors w.r.t. sequence length of proposed GFB-MRF method compared to the other methods on Brainweb digital phantom data with noisy measurements

the supported document were calculated. The most striking result was that the normalized std (i.e. std divided by the mean value) is around 4.5% for T1 (resp. 8.5% for T2) for the other methods and 3.4% for T1 (6.9% for T2) for GFB-MRF in the no-noise case. In the noisy case, the normalized std was way higher for other methods: around 8.5% for T1, (resp. between 22.4% and 25.7% for T2), while it staid at the same value of 3.5% for T1 (6.3% for T2) with GFB-MRF.

3.4. Volunteer data evaluations

In order to test the different methods on a realistic data, a volunteer data with B1 map was acquired using the sequence described in section 3.1 (i.e. a sequence of $L = 3000$ TRs retrospectively cropped to a length of $L = 1000$ TRs) on a MAGNETOM Prisma 3T MR scanner (Siemens Healthcare, Erlangen, Germany). A 20-channel head coil was used. Coil sensitivity maps were calculated following the method in [39] using the k-space central region (12×12) after gridding the temporal averaged MRF data.

The only thing that changes when using the B1 map compared to the case where there is no B1 map, was in the dictionary matching step. Each B1 value has its own fingerprint dictionary, and for each voxel the dictionary corresponding to the B1 value of that voxel is chosen in order to perform the matching.

Results on volunteer data without added noise are depicted in Figure 6. Results of the other methods look similar to each other, but results of our proposed GFB-MRF method look slightly smoother. Results on noisy data (cf section 3.2.2), depicted in Figure 7, show that GFB-MRF was able to remove the noise and obtained smoother maps, more similar to the noise-free reference maps than the other methods.

4. Discussion

We presented a new method for MRF which exploits jointly low-rank (via SVD compression), spatial (via TV regularization) and temporal regularizations (via Bloch manifold projection, i.e. fingerprint matching), into an iterative algorithm, to improve MRF reconstruction.

We presented and evaluated different variants of our algorithm. Experiments showed that better results were obtained with back-tracking step size compared to fixed step size (cf comparison between IGP-MRF-01 and IGP-MRF-01BT), that better results were obtained with matching at every iteration as opposed to not matching at every iteration (cf comparison between IGP-MRF-01BT and IGP-MRF-00). Experiments did not indicate that the low-rank approach via autocalibration was better than the classical approach consisting of just using the dictionary for the SVD compression. In a first variant the spatial regularization and the fingerprint matching are applied sequentially (IGP-MRF), in the second variant they are applied in parallel (GFB-MRF). Experiments showed that GFB-MRF obtained better results than IGP-MRF.

In the second part of the experiments, we only compared our best method i.e. GFB-MRF w.r.t. some methods of the state of the art. Experiments on real

data, showed that all the tested methods performed relatively well at a short sequence length of 1000 TRs, but only our proposed method was able to get rid of the noise when the measurements were contaminated with noise.

In terms of computational performance, all the methods were implemented in Matlab and were executed on a windows 7 platform with a dual CPU Intel Xeon 2.3GHz and 64 GB of RAM. Our proposed method took, for the Brainweb dataset, about 20s per iteration, plus an additional 8.5s overhead for the initialization, so for 10 iterations the overall runtime was about 210s in Matlab. It is slightly worse than kt-SVD-MRF which took 170s with our Matlab implementation. However, in terms of memory, our method took around only 5MB of memory to store the MRF data as opposed to around 768MB for kt-SVD-MRF because in our method, the data size is a matrix of size: number of pixels x dictionary compression ratio k , (i.e. roughly $(256)^2 \times 10 = 655'360$) which doesn't depend on the sequence length, while the data size of kt-SVD-MRF is: sequence length L x readout length x number of spirals (i.e. roughly $1000 \times 2000 \times 48 = 96'000'000$).

5. Conclusion

We presented a new method for MRF which is able to exploit efficiently low-rank, spatial and temporal regularizations, into an iterative algorithm, to improve MRF reconstruction. In order to regularize the images both spatially and temporally (via the Bloch manifold constraint), our algorithm applies these two regularizations in parallel as suggested by the generalized forward-backward algorithm. On the other hand, the low-rank regularization is imposed via an offline SVD compression so that no SVD is performed during the execution of the algorithm. The superiority of the proposed approach compared to state-of-the-art methods was demonstrated on Brainweb digital phantom data and scanned data. On Brainweb digital phantom data, we show that the average error of our proposed method is about two times smaller than the other methods for all the tested cases, i.e. for different sequence lengths (from 600 to 3000 TRs), with or without additional noise to the measurements. While the improvement on low-noise scanned data is difficult to assess, the proposed method was the only tested method that was able to reconstruct good-quality maps in case of measurements corrupted by noise.

We surmise that the gap in the performance between the results on digital phantom data and scanned data is due to the forward imaging model which do not take into account approximations in the k-space trajectory, motion, chemical shift, magnetic susceptibility, inhomogeneous B0 and B1 fields, etc. As a consequence, we think that the proposed method could be further improved by improving the forward imaging model used in our algorithm. One way to improve the model would be to replace some of the operators with trainable modules that learn to correct the model imperfections.

References

- [1] D. Ma, V. Gulani, N. Seiberlich, K. Liu, J. L. Sunshine, J. L. Duerk, M. A. Griswold, Magnetic resonance fingerprinting, *Nature* 495 (7440) (2013) 187–192.
- [2] B. Zhao, J. P. Haldar, K. Setsompop, L. L. Wald, Optimal experiment design for magnetic resonance fingerprinting, in: 2016 38th Annual International Conference of the IEEE Engineering in Medicine and Biology Society (EMBC), IEEE, 2016, pp. 453–456.
- [3] D. F. McGivney, E. Pierre, D. Ma, Y. Jiang, H. Saybasili, V. Gulani, M. A. Griswold, SVD compression for magnetic resonance fingerprinting in the time domain, *IEEE transactions on medical imaging* 33 (12) (2014) 2311–2322.
- [4] X. Cao, C. Liao, Z. Wang, Y. Chen, H. Ye, H. He, J. Zhong, Robust sliding-window reconstruction for accelerating the acquisition of mr fingerprinting, *Magnetic resonance in medicine* 78 (4) (2017) 1579–1588.
- [5] M. Davies, G. Puy, P. Vandergheynst, Y. Wiaux, A compressed sensing framework for magnetic resonance fingerprinting, *SIAM Journal on Imaging Sciences* 7 (4) (2014) 2623–2656.
- [6] C. C. Cline, X. Chen, B. Mailhé, Q. Wang, J. Pfeuffer, M. Nittka, M. A. Griswold, P. Speier, M. S. Nadar, AIR-MRF: Accelerated iterative reconstruction for magnetic resonance fingerprinting, *Magnetic resonance imaging* 41 (2017) 29–40.
- [7] Z. Wang, H. Li, Q. Zhang, J. Yuan, X. Wang, Magnetic resonance fingerprinting with compressed sensing and distance metric learning, *Neurocomputing* 174 (2016) 560–570.
- [8] B. Zhao, K. Setsompop, H. Ye, S. F. Cauley, L. L. Wald, Maximum likelihood reconstruction for magnetic resonance fingerprinting, *IEEE transactions on medical imaging* 35 (8) (2016) 1812–1823.
- [9] E. Y. Pierre, D. Ma, Y. Chen, C. Badve, M. A. Griswold, Multiscale reconstruction for mr fingerprinting, *Magnetic resonance in medicine* 75 (6) (2016) 2481–2492.
- [10] M. Doneva, T. Amthor, P. Koken, K. Sommer, P. Börnert, Matrix completion-based reconstruction for undersampled magnetic resonance fingerprinting data, *Magnetic Resonance Imaging* 41 (2017) 41–52.
- [11] B. Zhao, K. Setsompop, E. Adalsteinsson, B. Gagoski, H. Ye, D. Ma, Y. Jiang, P. Ellen Grant, M. A. Griswold, L. L. Wald, Improved magnetic resonance fingerprinting reconstruction with low-rank and subspace modeling, *Magnetic Resonance in Medicine* 79 (2) (2018) 933–942.

- [12] G. Mazor, L. Weizman, A. Tal, Y. C. Eldar, Low rank magnetic resonance fingerprinting, in: 2016 38th Annual International Conference of the IEEE Engineering in Medicine and Biology Society (EMBC), IEEE, 2016, pp. 439–442.
- [13] J. Assländer, M. A. Cloos, F. Knoll, D. K. Sodickson, J. Hennig, R. Lattanzi, Low rank alternating direction method of multipliers reconstruction for mr fingerprinting, *Magnetic resonance in medicine* 79 (1) (2018) 83–96.
- [14] A. Bustin, G. Lima da Cruz, O. Jaubert, K. Lopez, R. M. Botnar, C. Prieto, High-dimensionality undersampled patch-based reconstruction (hd-prost) for accelerated multi-contrast mri, *Magnetic resonance in medicine* 81 (6) (2019) 3705–3719.
- [15] G. Lima da Cruz, A. Bustin, O. Jaubert, T. Schneider, R. M. Botnar, C. Prieto, Sparsity and locally low rank regularization for mr fingerprinting, *Magnetic resonance in medicine* 81 (6) (2019) 3530–3543.
- [16] S. Arberet, X. Chen, B. Mailhé, P. Speier, M. S. Nadar, CS-MRF: Sparse & low-rank iterative reconstruction for magnetic resonance fingerprinting, in: ISMRM Workshop on Magnetic Resonance Fingerprinting, 2017.
- [17] S. Arberet, X. Chen, B. Mailhé, P. Speier, M. Nittka, H. Meyer, M. S. Nadar, GFB-MRF: Parallel spatial and bloch manifold regularized iterative reconstruction for magnetic resonance fingerprinting, in: Proc. 27th Sci. Meet. Int. Soc. Magn. Reson. Med., 2019.
- [18] D. P. Bertsekas, Incremental gradient, subgradient, and proximal methods for convex optimization: A survey, *Optimization for Machine Learning* 2010 (1-38) (2011) 3.
- [19] H. Raguét, J. Fadili, G. Peyré, A generalized forward-backward splitting, *SIAM Journal on Imaging Sciences* 6 (3) (2013) 1199–1226.
- [20] A. Chambolle, An algorithm for total variation minimization and applications, *Journal of Mathematical imaging and vision* 20 (1) (2004) 89–97.
- [21] U. S. Kamilov, E. Bostan, M. Unser, Variational justification of cycle spinning for wavelet-based solutions of inverse problems, *IEEE Signal Processing Letters* 21 (11) (2014) 1326–1330.
- [22] B. Mailhé, A. Ruppel, Q. Wang, M. S. Nadar, Fast and memory efficient redundant wavelet regularization with sequential cycle spinning, US Patent 9,858,689 (Jan. 2 2018).
- [23] S. F. Cauley, K. Setsompop, D. Ma, Y. Jiang, H. Ye, E. Adalsteinsson, M. A. Griswold, L. L. Wald, Fast group matching for MR fingerprinting reconstruction, *Magnetic resonance in medicine* 74 (2) (2015) 523–528.

- [24] M. Muja, D. Lowe, Flann-fast library for approximate nearest neighbors user manual, Computer Science Department, University of British Columbia, Vancouver, BC, Canada (2009).
- [25] O. Cohen, B. Zhu, M. Rosen, Deep learning for fast mr fingerprinting reconstruction, in: 2017 Scientific Meeting Proceedings. International Society for Magnetic Resonance in Medicine, 2017, p. 688.
- [26] Z. Fang, Y. Chen, M. Liu, L. Xiang, Q. Zhang, Q. Wang, W. Lin, D. Shen, Deep learning for fast and spatially constrained tissue quantification from highly accelerated data in magnetic resonance fingerprinting, *IEEE transactions on medical imaging* 38 (10) (2019) 2364–2374.
- [27] P. Song, Y. C. Eldar, G. Mazor, M. R. Rodrigues, Magnetic resonance fingerprinting using a residual convolutional neural network, in: ICASSP 2019-2019 IEEE International Conference on Acoustics, Speech and Signal Processing (ICASSP), IEEE, 2019, pp. 1040–1044.
- [28] High Precision Devices Inc., NIST phantom, Boulder, Colorado, USA (2016).
URL <http://www.hpd-online.com/MRI-phantoms.php>
- [29] J. A. Fessler, B. P. Sutton, Nonuniform fast fourier transforms using min-max interpolation, *IEEE transactions on signal processing* 51 (2) (2003) 560–574.
- [30] B. Recht, M. Fazel, P. A. Parrilo, Guaranteed minimum-rank solutions of linear matrix equations via nuclear norm minimization, *SIAM review* 52 (3) (2010) 471–501.
- [31] P. L. Combettes, J.-C. Pesquet, Proximal splitting methods in signal processing, in: Fixed-point algorithms for inverse problems in science and engineering, Springer, 2011, pp. 185–212.
- [32] T. Blumensath, M. E. Davies, Normalized iterative hard thresholding: Guaranteed stability and performance, *IEEE Journal of selected topics in signal processing* 4 (2) (2010) 298–309.
- [33] C. A. Cocosco, V. Kollokian, R. K.-S. Kwan, G. B. Pike, A. C. Evans, Brainweb: Online interface to a 3d MRI simulated brain database, *NeuroImage* 5 (4) (1997) 301–307.
- [34] E. Pierre, M. A. Griswold, A. Connelly, Fast analytical solution for extreme unaliasing of MRF image series, in: Proc. 25th Sci. Meet. Int. Soc. Magn. Reson. Med., 2017.
- [35] C. Meyer, L. Zhao, M. Lustig, M. Jilwan-Nicolas, M. Wintermark, J. Mugler, F. Epstein, Dual-density and parallel spiral asl for motion artifact reduction, in: Proc. Intl. Soc. Mag. Reson. Med, Vol. 19, 2011, p. 3986.

- [36] J. Pfeuffer, A. Kechagias, G. Kördörfer, D. Ma, M. Griswold, M. Nittka, Mitigation of spiral undersampling artifacts in magnetic resonance fingerprinting (mrf) by adapted interleaf reordering, in: Proceedings of the 25th Annual Meeting of ISMRM, Honolulu, Vol. 133, 2017.
- [37] S. S. Chen, D. L. Donoho, M. A. Saunders, Atomic decomposition by basis pursuit, SIAM review 43 (1) (2001) 129–159.
- [38] M. Griswold, J. Sunshine, N. Seiberlich, V. Gulani, Towards unified colormaps for quantitative MRF data, in: Proc. 26th Sci. Meet. Int. Soc. Magn. Reson. Med., 2018.
- [39] M. Uecker, P. Lai, M. J. Murphy, P. Virtue, M. Elad, J. M. Pauly, S. S. Vasanawala, M. Lustig, ESPIRiT-An eigenvalue approach to autocalibrating parallel MRI: where SENSE meets GRAPPA, Magnetic resonance in medicine 71 (3) (2014) 990–1001.

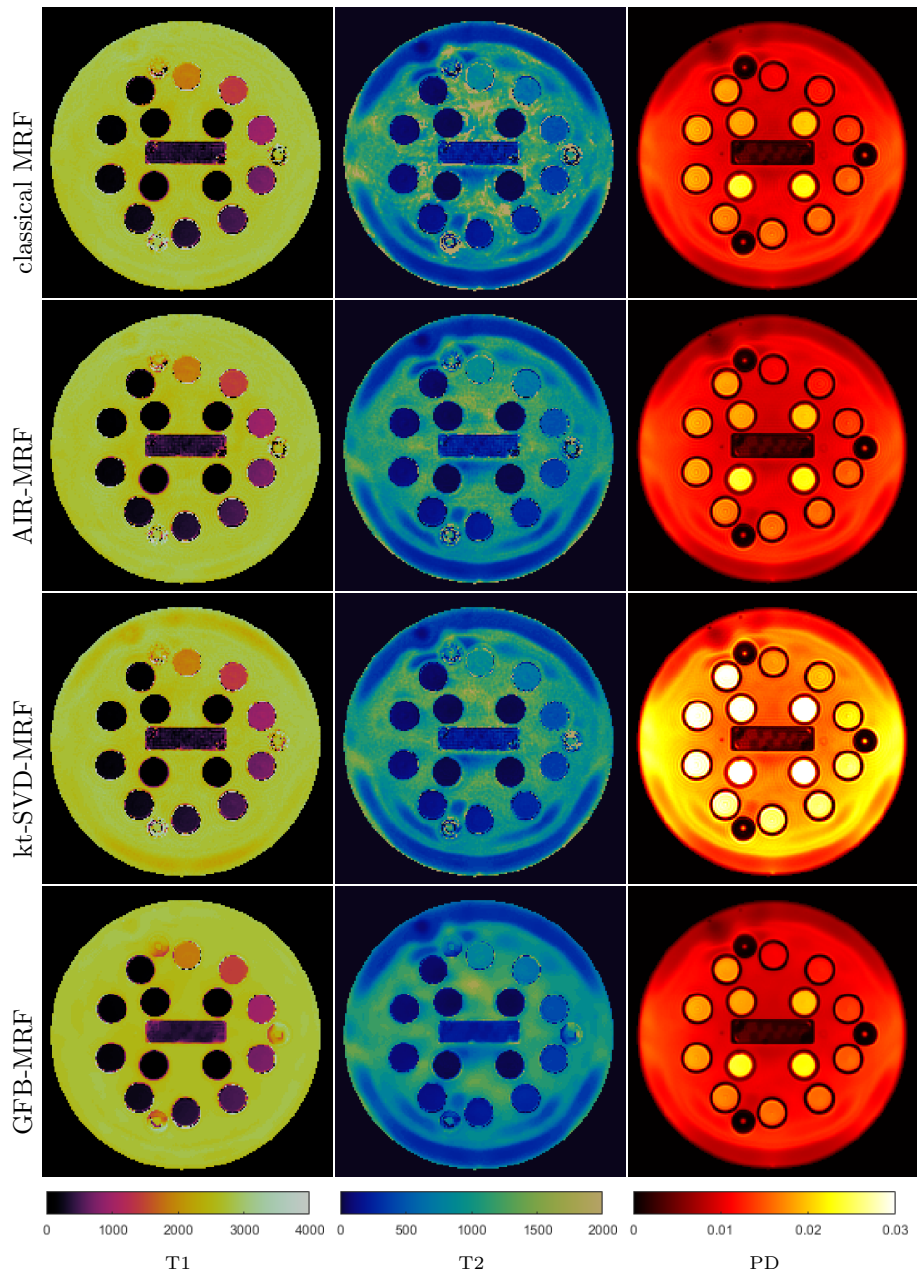


Figure 4: NIST phantom evaluations with noise-free measurements and sequence length 1000

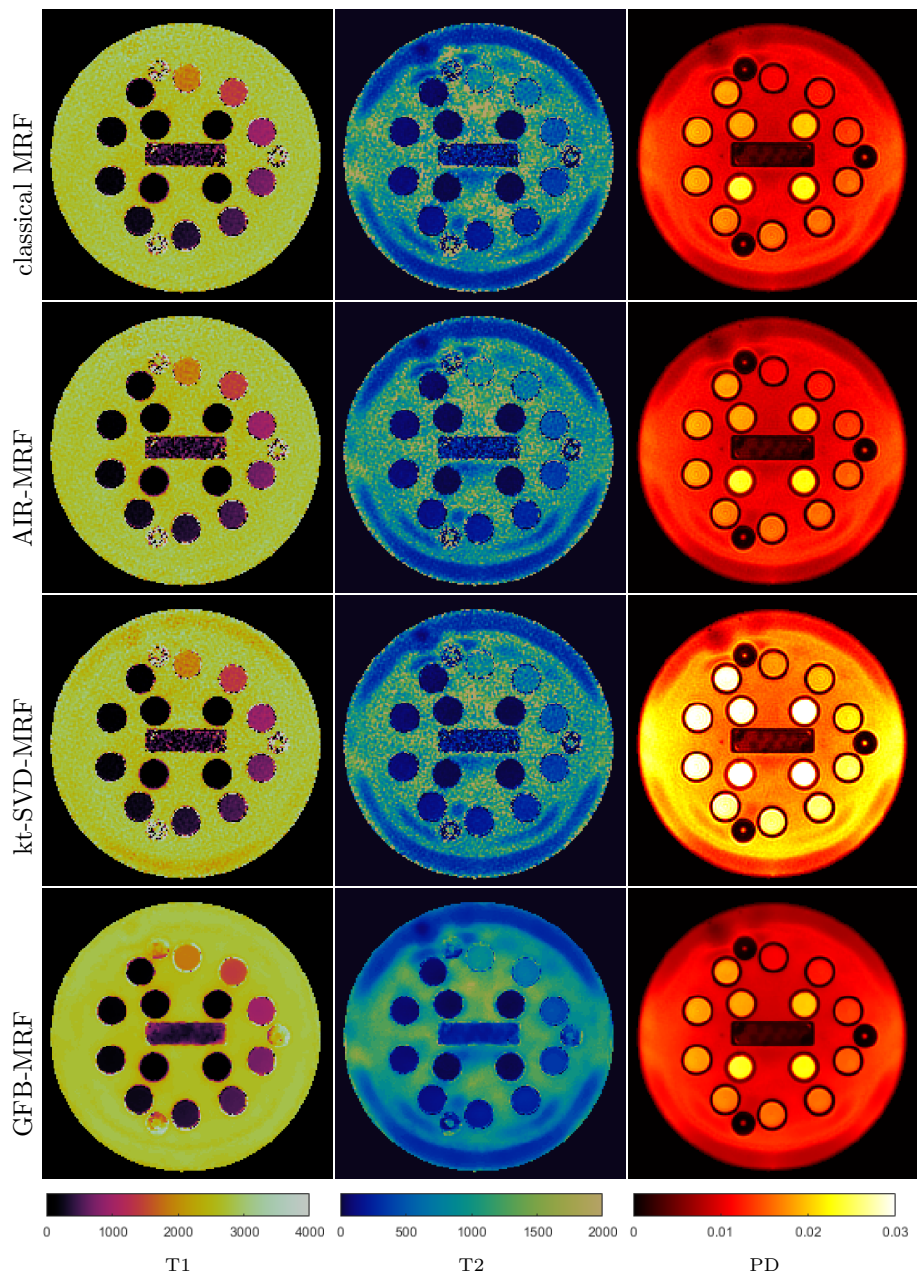


Figure 5: NIST phantom evaluations with noisy measurements and sequence length 1000

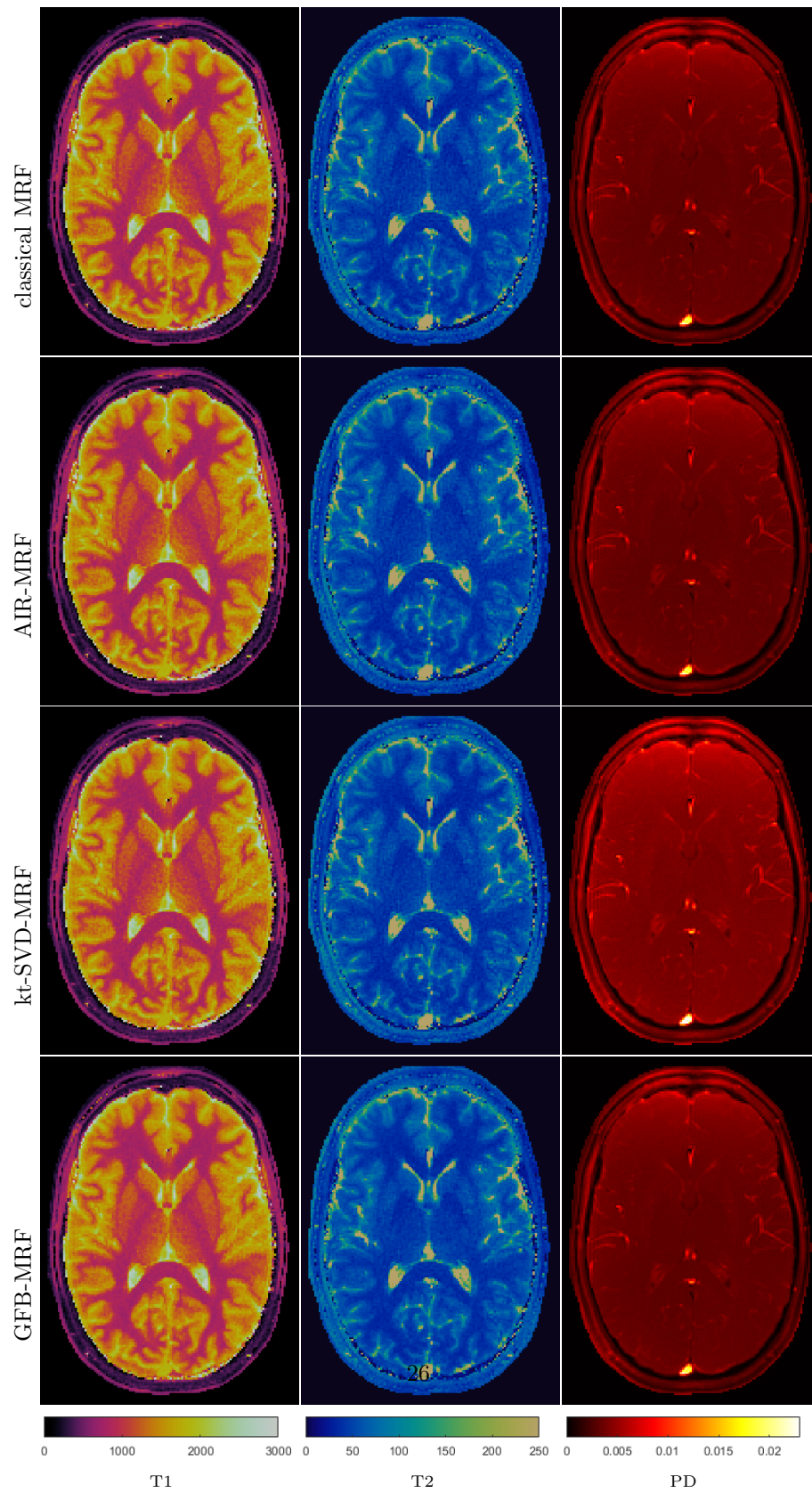


Figure 6: Volunteer data evaluations with noise-free measurements and sequence length 1000

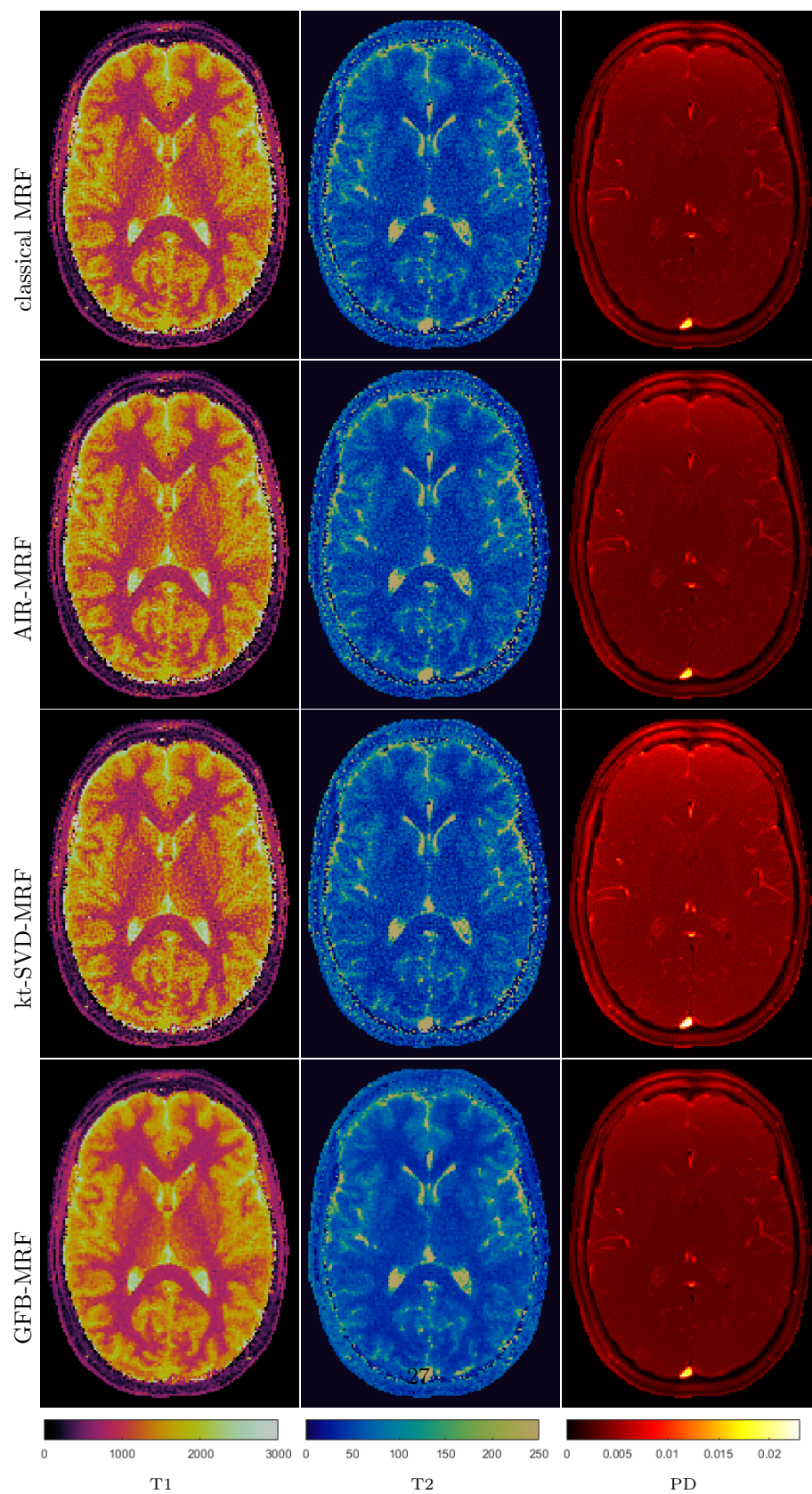


Figure 7: Volunteer data evaluations with noisy measurements and sequence length 1000